Efficient Detection for Multifrequency Dynamic Phasor Analysis

Guglielmo Frigo, Giada Giorgi and Claudio Narduzzi
Department of Information Engineering
University of Padova, Padova, Italy
{frigogug, giada, narduzzi}@dei.unipd.it

***Abstract*— Analysis of harmonic and interharmonic phasors is a promising smart grid measurement and diagnostic tool. This creates the need to deal with multiple phasor components having different amplitudes, including interharmonics with unknown frequency locations. The CSTFM algorithm [7] provides very accurate results under demanding test conditions, but is computationally demanding. In this paper we present a novel frequency search criterion with significantly improved effectiveness, resulting in a very efficient revised CSTFM algorithm.**

I. Introduction

Analysis of harmonic and interharmonic phasors is a promising measurement and diagnostic tool for power quality in smart grids, particularly in distribution networks. It is also a more demanding proposition than basic phasor measurement at the fundamental power system frequency, since processing requirements typically increase with phasor algorithm sophistication [1], evidencing the need for careful and efficient implementation to avoid too high computational load [2], [3].

In multifrequency analysis, problems are compounded by the need to deal with multiple phasor components with different amplitudes, possibly including interharmonics whose frequency location is, a priori, unknown [4]. This requires the addition of dedicated signal processing stages, emphasizing the importance of efficient algorithm development to keep computational load under control [5]. The algorithm proposed in [6], inspired by compressive sensing (CS) techniques, can effectively analyze a signal in terms of multifrequency phasors. Its evolution, the CS-based CSTFM algorithm [7], accurately estimates the Taylor-Fourier (TF) coefficients of multifrequency dynamic phasors under demanding test conditions, but is arguably one of the most computationally demanding in the literature. As a consequence, in its current implementation CSTFM is somewhat limited as far as reporting rates are concerned, in spite of its ability to employ comparatively short observation intervals (typical length is 5 cycles at the power system frequency, but as few as 3 cycles can be employed).

A review of CSTFM algorithm characteristics showed that, for multifrequency analysis, the current approach based on sequential detection of phasor components represents a significant performance bottleneck. This motivated our effort to find more efficient search criteria, by which multiple phasor frequencies could be located simultaneously. This in turn allows the estimation of TF coefficients for several phasor components in parallel, dramatically enhancing efficiency.

The purpose of this paper is to present a novel phasor detection criterion with significantly improved effectiveness, particularly in multifrequency phasor analysis. In the next Section, we shall briefly analyze relevant aspects of the CSTFM algorithm. We proceed then to introduce the search criterion, that allows to obtain a complete analysis in at most two iterations. In the final Section some results are provided to support and emphasize our claims about algorithm efficiency.

II. Multifrequency Dynamic Phasors and CSTFM

The multifrequency dynamic phasor model represents a generic waveform $x(t)$ by the sum of cisoidal components with time-varying amplitudes and phases:

$$x(t) = \frac{1}{\sqrt{2}} \sum_{f_h \in S_h} \bar{\mathbf{X}}_h(t) e^{j2\pi f_h t} + \bar{\mathbf{X}}_h^*(t) e^{-j2\pi f_h t} \qquad (1)$$

The time-varying complex function $\bar{\mathbf{X}}_h(t)$ is called a *dynamic phasor* and is referred to frequency f_h. The frequency set S_h includes the power system frequency, its harmonic multiples as well as some generic interharmonic frequencies. It should be emphasized that dynamic phasors in (1), as well as in (2) below, are referred to *actual* phasor frequencies. Since even the fundamental may deviate from its nominal value, they are all considered unknowns in a continuous range of values.

The CSTFM algorithm employs the representation of dynamic phasors by a Taylor series of order K, as introduced in [8]. This results in the Taylor-Fourier multifrequency (TFM) model:

$$x(t) = \frac{1}{\sqrt{2}} \sum_{f_h \in S_h} \sum_{k=0}^{K} \frac{t^k}{k!} \left(\mathbf{p}_h^{(k)} e^{j2\pi f_h t} + \mathbf{p}_h^{*(k)} e^{-j2\pi f_h t} \right) \qquad (2)$$

where complex TF coefficients $\mathbf{p}_h^{(k)}$ are the k-th order derivatives of $\bar{\mathbf{X}}_h(t)$ at $t = 0$.

We consider an acquisition interval length T_W and assume a sequence length of $2N+1$ samples, that is: $T_W = (2N+1)T_s$, where T_s is the sampling interval. Let

$$\underline{\mathbf{x}} = [x(-NT_s), \ldots, x(0), \ldots, x(NT_s)]^{\mathrm{T}} \qquad (3)$$

be the vector of signal samples acquired during an interval T_W. Use of the index range $-N \leq n \leq +N$ ensures the phase reference is the instantaneous phase at $n = 0$ for each phasor component.

The CSTFM algorithm introduces a discrete frequency grid $l\Delta_f$, with a fine step size $\Delta_f = 1/(T_W P)$ and an index range $-NP \le l \le +NP$, which yields $(2N+1)P$ evenly spaced grid points in the frequency range $[-\frac{1}{2T_s}, +\frac{1}{2T_s}]$. Accordingly, any phasor component frequency f_h can be approximated as:

$$\hat{f}_h \cong l_h \Delta_f, \qquad \text{with: } \left|\hat{f}_h - f_h\right| \le \frac{\Delta_f}{2}. \tag{4}$$

Integers l_h form the index set $S \subset \{-NP \dots 0 \dots +NP\}$ that, in principle, has the same number of elements as S_h.

As frequencies f_h are unknown, a vector of unknown TF coefficients can be associated to each index l as $\underline{\mathbf{p}}_l = [\mathbf{p}_l^{(0)}, \dots \mathbf{p}_l^{(K)}]^{\mathrm{T}}$. From these, a larger vector is created as: $\underline{\mathbf{p}} = [\underline{\mathbf{p}}_{-PN}^{\mathrm{T}} \ \dots \ \underline{\mathbf{p}}_0^{\mathrm{T}} \ \dots \ \underline{\mathbf{p}}_{+PN}^{\mathrm{T}}]^{\mathrm{T}}$. Application of Fourier transform properties allows to write the TFM model as a linear matrix equation in the unknown $\underline{\mathbf{p}}$ [7]:

$$\underline{\mathbf{x}} = \mathbf{W}^{\mathrm{H}} \mathbf{D} \underline{\mathbf{p}} + \underline{\mathbf{e}} \tag{5}$$

where matrices $\mathbf{W}$ and $\mathbf{D}$ are defined in Appendix A. Vector $\underline{\mathbf{e}}$ represents data acquisition system uncertainty and noise, as well as model uncertainty. The CSTFM algorithm estimates TF coefficents in (2) as the *sparse* solution of (5):

$$\hat{\underline{\mathbf{p}}} = \arg\min_{\underline{\mathbf{p}}} \|\underline{\mathbf{p}}\|_0 \qquad \text{subject to: } \|\underline{\mathbf{x}} - \mathbf{W}^{\mathrm{H}} \mathbf{D} \underline{\mathbf{p}}\|_2 \le \zeta. \tag{6}$$

Here, $\|\underline{\mathbf{p}}\|_0$ indicates the number of non-zero elements of $\underline{\mathbf{p}}$.

The full algorithm, in the form proposed in [7], is presented in Appendix B for completeness. It relies on an orthogonal matching pursuit (OMP) approach [12], that consists in the sequential determination of frequency indexes in the set S by the iterative execution of two alternate stages: index detection and phasor estimation. According to the discussion in Appendix B, computational complexity of each iteration is slightly more than linear in the number of samples $(2N+1)$. However, multifrequency phasor analysis requires as many OMP iterations as the number of phasor components, which makes the total computational burden very high in the case of multifrequency analysis. Furthermore, algorithm duration is non-deterministic, since termination criteria, based either on the threshold ζ in (6) or on a maximum number of iterations depend on the characteristics of the signal itself.

These limitations explain the need for a more effective frequency search algorithm and the move to parallel estimation of multiple phasor components, that will be presented in the following Sections.

III. Preliminary Remarks on Phasor Detection

We focus here on the detection of the frequency indexes of phasor components, referring to equations (16) and (17) in Appendix B. Indicating by $X(\nu)$ the discrete-time Fourier transform of $\underline{\mathbf{x}}$, it follows from (17) that the first iteration finds the largest peak of $|X(\nu) \circledast D(\nu)|$ and the index points to the closest frequency on the discrete grid. In practice, this will be the contribution of the phasor at the fundamental frequency.

It may seem easy to also find harmonic frequencies, by searching for relative peaks of $|X(\nu) \circledast D(\nu)|_{\nu = l\Delta_f}$ within predictable intervals. Unfortunately, the Dirichlet kernel (13), also called a rectangle (or uniform) window, contributes very significant sidelobes, preventing detection of any other phasor component. In fact, harmonic amplitudes are expected to be just a few percent of the fundamental or even less, whereas the largest sidelobe of $D(\nu)$ is about 20% of the mainlobe (-13 dB) and sidelobe magnitudes only decay in proportion to $\frac{1}{\nu}$ (basic features are summarized, for instance, in [10]).

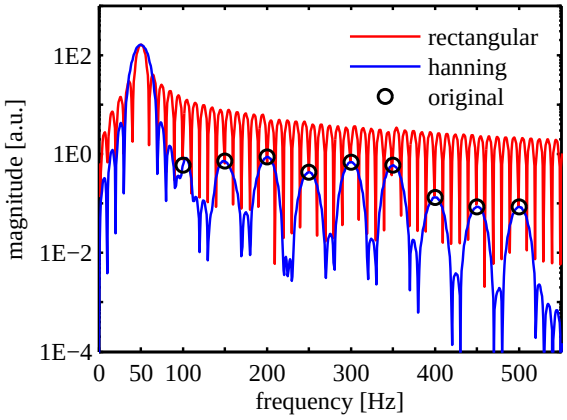

Fig. 1. Comparison between the amplitude spectrum $|X(\nu) \circledast D(\nu)|$ obtained by using an implicit rectangular window (red) and $|X(\nu) \circledast W_H(\nu)|$, obtained with a Hanning window (blue). Harmonic component magnitudes are identified by black circles.

The situation is depicted by the red line in Fig. 1, that refers to the amplitude spectrum of a waveform with 1% total harmonic distortion. Only the fundamental component, corresponding to the largest peak, can be correctly detected. Harmonic components (indicated by black circles) are hidden by Dirichlet side lobes associated with the fundamental, but their detection becomes possible if the estimation residual is searched. Apparently this leaves iterative frequency search, according to (16), as the only viable approach.

A very effective alternative can be realized by allowing some freedom from the CSTFM mathematical framework in the phasor detection process. Following a well-known practice in spectral analysis, we simply introduce a window function to reduce spectral interference among frequency components. The result obtained by applying a Hanning window $W_H(\nu)$ to the acquired signal samples is shown by the blue line in Fig. 1, which shows $|X(\nu) \circledast W_H(\nu)|$. The largest sidelobe of $W_H(\nu)$ is about 2.5% of the mainlobe (-32 dB) and side lobe decay is proportional to $\frac{1}{\nu^3}$ [10], thus reducing spectral leakage and, consequently, interference among neighbouring spectral components. Local peaks are clearly detectable and their positions nearly coincide with the reference.

This enables the estimation of harmonic frequencies already during the first step of the CSTFM algorithm. Accordingly, we developed a very efficient frequency search criterion that allows enhanced multifrequency analysis of dynamic phasors, as will be shown in the following Sections.

IV. Efficient algorithm implementation

The modified CSTFM algorithm consists of just two iterations, whose duration is almost independent of signal properties. Initial conditions are the same as in the original algorithm, with an initially empty index set: $S(0) = \varnothing$.

A. First iteration

1) Index detection: This step is carried out in two stages:

a) Detection of the fundamental component: this stage consists in finding the index $l_1(1)$ such that:

$$l_1(1) = \arg \max_{l_{1,\downarrow} \le l < l_{1,\uparrow}} \|(\mathbf{D}_l^{(0)})^{\mathrm{H}} \mathbf{W} \underline{\mathbf{x}}_{hann}\|_2, \qquad (7)$$

where $\underline{\mathbf{x}}_{hann}$ is obtained by weighting the acquired samples $\underline{\mathbf{x}}$ with the corresponding Hanning weights. Search interval bounds $l_{1,\downarrow}$ and $l_{1,\uparrow}$ depend on the allowed range of variability for the fundamental frequency. Considering a $\pm 10\%$ variation from the nominal value f_0: $l_{1,\downarrow} = \lfloor \frac{0.9 f_0}{\Delta_f} \rfloor$ and $l_{1,\uparrow} = \lceil \frac{1.1 f_0}{\Delta_f} \rceil$.

b) Detection of harmonic components: the second stage consists of local searches, within the same set of values as in (7), for possible harmonic components. The *candidate* peak location index corresponding to the h-th harmonic is:

$$l_h(1) = \arg \max_{l_{h,\downarrow} < l < l_{h,\uparrow}} \|(\mathbf{D}_l^{0})^{\mathrm{H}} \mathbf{W} \underline{\mathbf{x}}_{hann}\|_2, \qquad (8)$$

where the lower and upper bounds are: $l_{h,\downarrow} = h \cdot (l(1) - \Delta_l)$ and $l_{h,\uparrow} = h \cdot (l(1) + \Delta_l)$. The search range width $2\Delta_l$ is related to the accuracy associated to the estimate $l_1(1)$, therefore very small index subsets need to be considered, drastically reducing the number of comparisons.

Repeating the operation is for $h = 2$ to H, where $(H-1)$ is the maximum number of harmonics under analysis, yields a candidate index set. It is now essential to discriminate possible ambiguities caused by Hanning window side-lobes of the fundamental component. For this reason, we introduce a *frequency-dependent* threshold that follows Hanning side-lobe amplitude decay. If peak amplitude at frequency $l_h(1)\Delta_f$ is lower than the corresponding threshold, $l_h(1)$ is discarded.

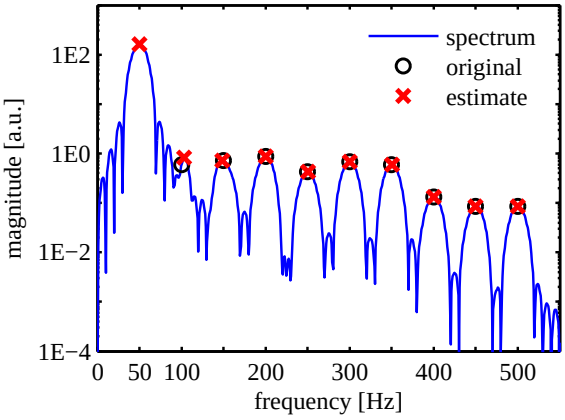

Fig. 2. Harmonic components estimated by the two-stage index detection step. Peaks associated to Hanning window side lobes are, correctly, ignored.

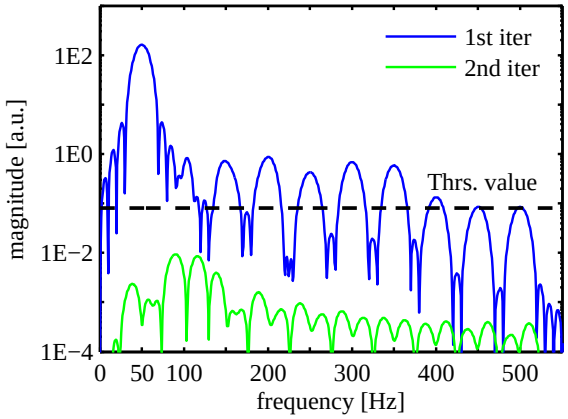

Fig. 3. Amplitude spectrum of residual $\underline{\mathbf{r}}(1)$ (in green), compared with the amplitude spectrum of Fig. 2. No component exceeds the given threshold ρ.

The detection step produces an updated index set $S(1) = S(0) \cup \{l_1(1)\} \cup \{l_h(1) : h \in H^*\}$, with subset $H^* \subset \{2, \ldots, H\}$ containing the harmonics that passed the check. Results for the example of Fig. 1 are shown in Fig. 2.

2) Phasor estimation: This step is similar to phasor estimation described in Appendix B, but in this case we start at once with multiple components. The reduced matrix $\mathbf{D}_{S(1)}$ is the concatenation of all submatrices referred to detected indexes:

$$\mathbf{D}_{S(1)} = \left[\mathbf{D}_l^{(K)}\right]_{l \in S(1)}. \qquad (9)$$

In agreement with (18), the least-squares estimate $\underline{\hat{\mathbf{p}}}(1)$ is:

$$\underline{\hat{\mathbf{p}}}(1) = \left[(\mathbf{D}_{S(1)})^{\mathrm{H}} \mathbf{D}_{S(1)}\right]^{-1} (\mathbf{D}_{S(1)})^{\mathrm{H}} \underline{\mathbf{x}}. \qquad (10)$$

Signal reconstruction $\underline{\hat{\mathbf{x}}}(1) = \mathbf{W}^{\mathrm{H}} \mathbf{D} \underline{\hat{\mathbf{p}}}(1)$ is then subtracted from the measurement vector $\underline{\mathbf{x}}$ to obtain the residual $\underline{\mathbf{r}}(1)$.

B. Second iteration

In the second iteration the algorithm searches the residual $\underline{\mathbf{r}}(1)$ for further possible components. Any local maximum within $0 < l < NP$ exceeding a threshold ρ is considered:

$$l_m(2) = \arg \max_{l_{m,\downarrow} < l < l_{m,\uparrow}} \left[\|(\mathbf{D}_l^{0})^{\mathrm{H}} \mathbf{W} \underline{\mathbf{r}}_{hann}(1)\|_2 - \rho\right], \qquad (11)$$

Vector $\underline{\mathbf{r}}_{hann}(1)$ contains the Hanning weighted elements of $\underline{\mathbf{r}}(1)$ and $(\mathbf{D}^{0})^{\mathrm{H}} \mathbf{W} \underline{\mathbf{r}}_{hann}(1)$ corresponds to its zero-padded DFT, shown in Fig. 3 by the green line.

Indicating by M^* the subset of indices detected during this iteration, the new index set $S(2)$ is then obtained as $S(2) = S(1) \cup \{l_m(2) : m \in M^*\}$. Computation of the least squares estimate:

$$\underline{\hat{\mathbf{p}}}(2) = \left[(\mathbf{D}_{S(2)})^{\mathrm{H}} \mathbf{D}_{S(2)}\right]^{-1} (\mathbf{D}_{S(2)})^{\mathrm{H}} \underline{\mathbf{x}}. \qquad (12)$$

completes the algorithm.

V. Results

A. Analysis in the presence of inter-harmonics

In this example we evaluate the effectiveness of the proposed algorithm in the presence of harmonic and inter-harmonic disturbances. We set sampling rate to 5 kHz and consider a 50-Hz fundamental component with amplitude 230 a.u. and initial phase 0 rad. We assume a sequence length of $(2N+1) = 501$ samples, corresponding to approximately 5 periods of the fundamental component. A 1% total harmonic distortion is reproduced by generating harmonic components between 100 and 500 Hz, with amplitude and phase values randomly taken from Gaussian distributions. Considering a reporting rate of 50 Hz, phasor measurement passband defined in [11] is the interval [25, 75] Hz and, accordingly, we located two inter-harmonic components just outside the passband, at 11.62 and 75.24 Hz, respectively. Amplitudes and initial phases for these components are also pseudo-random Gaussian variables, producing an additional 1% overall inter-harmonic distortion. Finally, we model uncertainty sources inherent to the acquisition stage by additive white Gaussian noise corresponding to a signal-to-noise ratio of 80 dB.

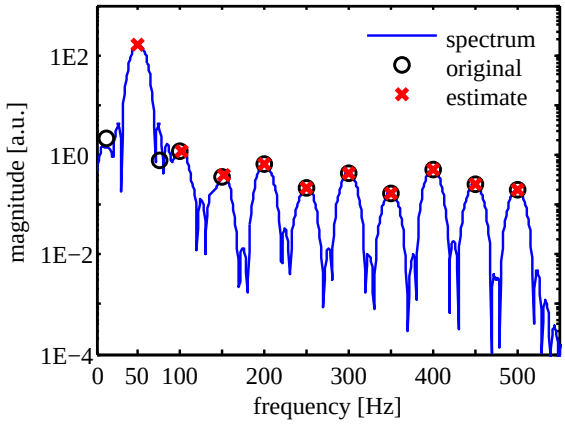

(a)

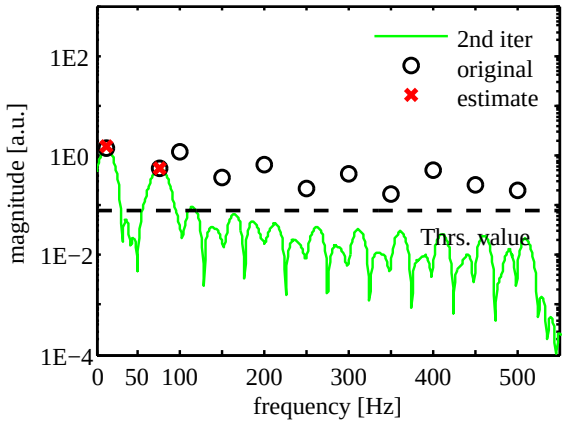

(b)

Fig. 4. Phasor components detection by the revised CSTFM algorithm. In the first iteration (a), the enhanced search criterion identifies harmonic components. In the second iteration (b), interharmonic components are detected.

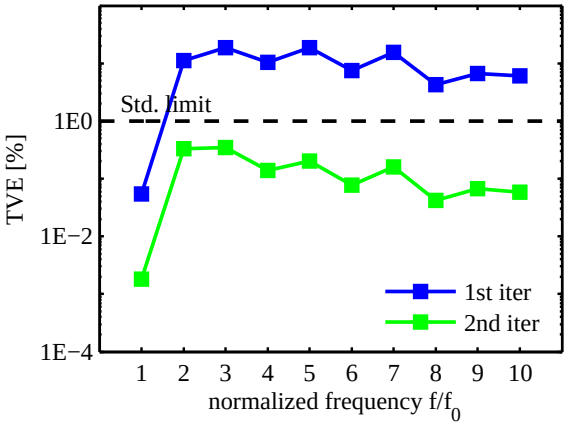

Fig. 5. Iterative enhancement of TVE. The first iteration (blue) considers only the harmonic contribution, the second one (green) also accounts for interharmonics and provides TVE $\leq 1\%$ for all considered components.

As shown in Fig. 4(a), the algorithm first iteration succeeds in identifying all harmonic components. whereas inter-harmonic components are masked by the fundamental main lobe. They are correctly identified in the second iteration from the residual $\underline{\mathbf{r}}(1)$, as shown in Fig. 4(b).

It should be noted that components identified in the first iteration are not entirely removed from $\underline{\mathbf{r}}(1)$. To avoid the risk of detecting their spurious contributions in the second iteration, we determined a pre-defined range of values for the threshold level ρ. The lower bound is given by the expected noise floor, while the upper bound depends on the desired level of sensitivity. In the present case, the threshold is set to 2.5×10^{-3} of the estimated fundamental component amplitude. Accordingly, only interharmonics not lower than 0.5% of the fundamental amplitude can be detected.

The two iterations of the enhanced CSTFM algorithm are sufficient to identify all significant components and compute the associated dynamic phasors. In Fig. 5, we report phasor estimation accuracy at the end of each iteration, in terms of total vector error (TVE), for the fundamental and harmonic components. After the first iteration the TFM model only includes the fundamental and harmonics. The resulting TVEs (blue line) suffer from the interfence coming from the two interharmonic components. At the end of the second iteration, instead, the multifrequency model accounts for all distortion contributions. Consequently, estimation accuracy improves and TVE not exceeding 1% is achieved for all harmonics, while fundamental component TVE is as low as 0.01%.

B. Analysis with shorter measurement interval – 3 cycles

In the second example, we evaluate the algorithm effectiveness with a shorter observation interval. We retain the same sampling rate as before, but sequence length is shorter, namely, $(2N+1) = 301$ samples, corresponding to approximately 3 periods of the fundamental component.

Component detection outcomes at the first iteration are shown in Fig. 6. Although frequency resolution is reduced, the

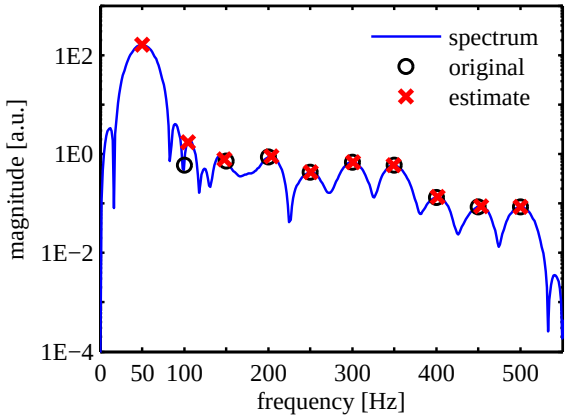

Fig. 6. Phasor detection for the signal of Fig. 4 with a shorter observation interval of 3 fundamental periods.

enhanced CSTFM algorithm is still able to detect all harmonic components. With a shorter observation interval, window lobe widths increase, making detection harder for inter-harmonics and for components closer to the fundamental. For instance, in this case the second harmonic is subjected to interference from the second and third side-lobes of the fundamental component, nevertheless the enhanced search criterion is still able to detect it, so that it can be included in the TFM model.

No contribution in the spectrum of $\underline{\mathbf{r}}(1)$ exceeds the second iteration threshold, as in this case no interharmonics are included in the synthesized waveform.

In Fig. 7 we compare TVEs associated to fundamental and harmonic waveform components, with measurement intervals corresponding to three and five periods at the nominal power system frequency. Since the TFM model is sufficiently exhaustive, the algorithm provides comparable TVE performance in the two cases. Therefore, it is reasonable to claim that harmonics can be detected even in a three-period interval, whereas five periods are recommended for inter-harmonics in the neighbourhood of the fundamental phasor component.

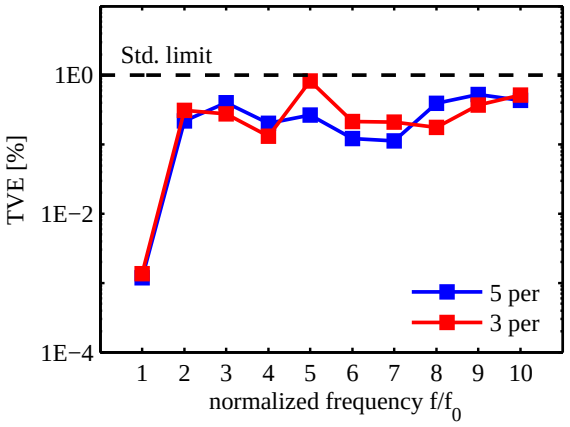

Fig. 7. TVE comparison for different observation interval lengths.

TABLE I

CSTFM COMPUTATION TIME COMPARISON

Test conditions	**Enhanced** time [s]	**OMP min** time [s]	**OMP total** time [s]
$T_W \cong 3$ periods, harmonics	0.051	0.495	0.572
$T_W \cong 5$ periods, harmonics	0.059	1.145	3.429
$T_W \cong 5$ per., harm. + IH	0.118	1.439	3.492

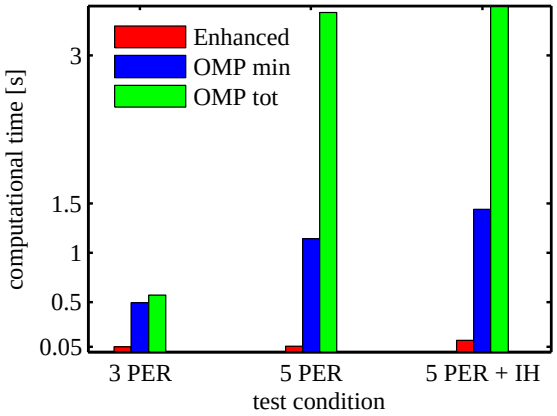

Fig. 8. Computation times in the three considered test conditions. The proposed method (red) has a nearly constant computation time, much lower than the traditional OMP approach if the ideal minimum number (blue) or the actual number (green) of iterations is considered.

C. Computational cost

Computational costs of the CSTFT algorithm for the OMP-based implementation and for the enhanced version proposed in this paper are compared in Table I and, graphically, in Fig. 8. Computation times refer to execution of Matlab 2012b code, running on a 2.1 GHz Intel processor. Relative comparison clearly demonstrates the efficiency of the proposed solution, that is faster by at least one order of magnitude. Actual times can be further reduced by code optimization and/or by a FPGA implementation.

VI. CONCLUSION

We have shown that the enhancements to the CSTFM algorithm proposed in this paper have a significant impact both on computational efficiency and on the ability to detect and accurately measure multiple phasor components. Furthermore, we provide further evidence that a CS-based approach allows to significantly reduce measurement intervals without affecting accuracy, which is beneficial in terms of reporting rates.

The enhanced CSTFM algorithm can be employed to implement a device having the flexibility to operate as a phasor measurement unit, as a harmonic phasor and power quality analyzer and, possibly, even as a protection relay, in an innovative and cost-effective way.

ACKNOWLEDGMENT

This research is wholly funded by the University of Padua and is a contribution to the European Metrology Research Programme (EMRP) Joint Research Project “Smart Grids II”.

REFERENCES

[1] A. Roscoe, "Exploring the relative performance of frequency-tracking and fixed-filter phasor measurement unit algorithms under C37.118 test procedures, the effects of interharmonics, and initial attempts at merging P-class response with M-class filtering," *Instrumentation and Measurement, IEEE Transactions on*, vol. 62, no. 8, pp. 2140–2153, Aug. 2013.

[2] P. Romano and M. Paolone, "Enhanced interpolated-DFT for synchrophasor estimation in FPGAs: Theory, implementation, and validation of a PMU prototype," *IEEE Trans. Instrum. Meas.*, vol. 63, no. 12, pp. 2824–2836, Dec. 2014.

[3] P. Castello, J. Liu, C. Muscas, P. A. Pegoraro, F. Ponci, and A. Monti, "A fast and accurate PMU algorithm for P+M class measurement of synchrophasor and frequency," *IEEE Trans. Instrum. Meas.*, vol. 63, no. 12, pp. 2837–2845, Dec. 2014.

[4] M. Chakir, I. Kamwa, and H. Le Huy, "Extended C37.118.1 PMU algorithms for joint tracking of fundamental and harmonic phasors in stressed power systems and microgrids," *IEEE Trans. Power Del.*, vol. 29, no. 3, pp. 1465–1480, Jun. 2014.

[5] C. Orallo, I. Carugati, S. Maestri, P. Donato, D. Carrica, and M. Benedetti, "Harmonics measurement with a modulated sliding discrete Fourier transform algorithm," *IEEE Trans. Instrum. Meas.*, vol. 63, no. 4, pp. 781–793, Apr. 2014.

[6] M. Bertocco, G. Frigo, C. Narduzzi, and F. Tramarin, "Resolution enhancement by compressive sensing in power quality and phasor measurement," *IEEE Trans. Instrum. Meas.*, vol. 63, no. 10, pp. 2358–2367, Oct. 2014.

[7] M. Bertocco, G. Frigo, C. Narduzzi, C. Muscas, and P. A. Pegoraro, "Compressive sensing of a Taylor-Fourier Multifrequency model for synchrophasor estimation," *IEEE Trans. Instrum. Meas.*, vol. 64, no. 12, pp. 3274–3283, Dec. 2015.

[8] J. A. de la O Serna, "Dynamic phasor estimates for power system oscillations," *IEEE Trans. Instrum. Meas.*, vol. 56, no. 5, pp. 1648–1657, Oct. 2007.

[9] M. A. Platas-Garza and J. A. de la O Serna, "Dynamic harmonic analysis through Taylor-Fourier transform," *IEEE Trans. Instrum. Meas.*, vol. 60, no. 3, pp. 804–813, Mar. 2011.

[10] F. Harris, "On the use of windows for harmonic analysis with the discrete Fourier transform," *Proc. IEEE*, vol. 66, no. 1, pp. 172–204, Jan. 1978.

[11] *IEEE Standard for Synchrophasor Measurements for Power Systems*, IEEE Std C37.118.1-2011 (Revision of IEEE Std C37.118-2005), Dec. 2011.

[12] J. Tropp and A. Gilbert, "Signal recovery from random measurements via orthogonal matching pursuit," *Information Theory, IEEE Transactions on*, vol. 53, no. 12, pp. 4655–4666, Dec 2007.

APPENDIX

A. Definition of matrices $\mathbf{W}$ and $\mathbf{D}$

The two matrices employed in equation (5) are defined as follows. Matrix $\mathbf{W}$ is a $(2N+1)\times(2N+1)$ orthogonal matrix, defined so that the columns of $\mathbf{W}^{\mathrm{H}}$ are the vectors of the basis set for the discrete Fourier transform (DFT). One has: $\mathbf{W}\mathbf{W}^{\mathrm{H}} = \mathbf{W}^{\mathrm{H}}\mathbf{W} = \frac{1}{2N+1}\mathbb{I}_{2N+1}$, where $\mathbb{I}$ is the identity.

To construct matrix $\mathbf{D}$ we first recall the Dirichlet kernel:

$$D_N(\nu) = \frac{\sin \pi(2N+1)\nu}{\sin \pi\nu}, \tag{13}$$

where $\nu = fT_s$ is a normalized frequency.

For each frequency index l, we define a submatrix $\mathbf{D}_l^{(K)}$ with size $(2N+1)\times(K+1)$ whose elements are:

$$\mathbf{D}_l^{(K)} = \begin{bmatrix} D_{-N,l}^{(0)} & D_{-N,l}^{(1)} & \dots & D_{-N,l}^{(K)} \\ \vdots & \vdots & & \vdots \\ D_{0,l}^{(0)} & D_{0,l}^{(1)} & \dots & D_{0,l}^{(K)} \\ \vdots & \vdots & & \vdots \\ D_{+N,l}^{(0)} & D_{+N,l}^{(1)} & \dots & D_{+N,l}^{(K)} \end{bmatrix} \tag{14}$$

where $D_{m,l}^{(k)}$ is the k-th order derivative of the Dirichlet kernel computed for: $\nu = \frac{m}{N} - \frac{l}{P(2N+1)}$. Matrix $\mathbf{D}$ is formed as:

$$\mathbf{D} = \left[\mathbf{D}_{-PN}^{(K)} \ \dots \ \mathbf{D}_0^{(K)} \ \dots \ \mathbf{D}_{+PN}^{(K)}\right]. \tag{15}$$

B. OMP Algorithm

The orthogonal matching pursuit (OMP) algorithm [12] progressively builds up a set $S(i)$ of identified frequency indexes l_h and a corresponding estimate $\hat{\underline{\mathbf{p}}}(i)$, where i is the iteration index. In the following we indicate by $\mathbf{D}_{S(i)}$ the reduced matrix composed only by submatrices $\mathbf{D}_l^{(K)}$ with $l \in S(i)$.

Given the estimate $\hat{\underline{\mathbf{p}}}(i)$ at the i-th iteration, the corresponding signal reconstruction is $\hat{\underline{\mathbf{x}}}(i) = \mathbf{W}^{\mathrm{H}}\mathbf{D}\hat{\underline{\mathbf{p}}}(i)$ and the approximation residual is defined as: $\underline{\mathbf{r}}(i) = \underline{\mathbf{x}} - \hat{\underline{\mathbf{x}}}(i)$. Initially S is an empty set $S(0) = \varnothing$, hence $\mathbf{D}_{S(0)}$ has zero columns, $\underline{\mathbf{p}}(0) = \underline{\mathbf{0}}$ and the initial signal reconstruction is $\hat{\underline{\mathbf{x}}}(0) = \underline{\mathbf{0}}$, so that the residual initial value is $\underline{\mathbf{r}}(0) = \underline{\mathbf{x}}$.

The two alternating iteration steps are:

1) Index detection: In the first step, index $l(i)$ is found as:

$$l(i) = \arg \max_{0 \le l < +PN} \|(\mathbf{D}_l^0)^{\mathrm{H}}\mathbf{W}\underline{\mathbf{r}}(i-1)\|_2, \tag{16}$$

and the support set is updated: $S(i) = S(i-1) \cup \{l(i)\}$.

Only *zero-order* submatrices $\mathbf{D}^0$ are considered in (16), as this suffices to locate the index of a phasor component and helps reduce computations. From definitions in Appendix A:

$$\|(\mathbf{D}_l^0)^{\mathrm{H}}\mathbf{W}\underline{\mathbf{r}}(i-1)\|_2 = |R_{i-1}(\nu) \circledast D(\nu)|_{\nu = l\Delta_f} \tag{17}$$

where $R_{i-1}(\nu)$ is the discrete-time Fourier transform of the elements of $\underline{\mathbf{r}}(i-1)$ and $\circledast$ denotes convolution. Therefore, (17) can be efficiently obtained from the DFT of $\underline{\mathbf{r}}(i-1)$ with a zero-padding factor P. This step thus requires $\mathrm{O}((2N+1)(\log(2N+1+2P-1))$ operations, followed by a peak search.

2) Phasor estimation: Next, an updated reduced matrix $\mathbf{D}_{S(i)} = \left[\mathbf{D}_{S(i-1)}\ \mathbf{D}_{l(i)}^{(K)}\right]$ is employed to obtain a new estimate by solving the reduced system $\underline{\mathbf{x}} = \mathbf{W}^{\mathrm{H}}\mathbf{D}_{S(i)}\underline{\mathbf{p}}(i)$. This yields:

$$\hat{\underline{\mathbf{p}}}(i) = \left[(\mathbf{D}_{S(i)})^{\mathrm{H}}\mathbf{D}_{S(i)}\right]^{-1}(\mathbf{D}_{S(i)})^{\mathrm{H}}\underline{\mathbf{x}}. \tag{18}$$

Signal reconstruction $\hat{\underline{\mathbf{x}}}(i) = \mathbf{W}^{\mathrm{H}}\mathbf{D}\hat{\underline{\mathbf{p}}}(i)$ is then subtracted from the measurement vector $\underline{\mathbf{x}}$ to obtain $\underline{\mathbf{r}}(i)$.

In this step the number of non-zero elements of $\hat{\underline{\mathbf{p}}}(i)$ increases with each iteration, in fact one has: $\|\hat{\underline{\mathbf{p}}}(i)\|_0 = (K+1)\cdot i$. Therefore, computational load also depends on i, with the inverse in (12) requiring $\mathrm{O}\big([(K+1)\cdot i]^3\big)$ operations. Completing the pseudoinverse computation requires a further $\mathrm{O}\big((2N+1)\cdot[(K+1)\cdot i]^2\big)$ operations and, finally, operations needed to find the current residual are $\mathrm{O}((2N+1)\cdot[(K+1)\cdot i])$.